



Article

Discrete Element Simulation of the Road Slope Considering Rainfall Infiltration

Xiao Gu ¹, Wen Nie ^{2,*}, Qihang Li ³, Jiabo Geng ¹, Tao Zhou ¹ and Canming Yuan ²

¹ School of Emergency Management and Safety Engineering, Jiangxi University of Science and Technology, Ganzhou 341000, China

² School of Resource and Environment Engineering, Jiangxi University of Science and Technology, Ganzhou 341000, China

³ School of Resources and Safety Engineering, Chongqing University, Chongqing 400044, China

* Correspondence: wen.nie@vip.tom.com

Abstract: Rainfall infiltration is the primary factor that induces landslides. In this paper, discrete element software (PFC^{3D}) was used to establish a novel rainfall infiltration model, which integrates water transfer, intensity decay and seepage force into the calculation of the moisture field. By applying this model to the rainfall infiltration analysis of a road slope in Nanping City, Fujian Province, China, the distribution law of water content, the functional relationship between shear strength and water content, and the calculation of permeability at different times can be obtained. The model was verified by comparing simulated results of water content with field monitoring data. The simulation error of water content is lower than 10%. Furthermore, this model application was validated by reproducing the pressure variation of the retaining wall on 12 May 2022. To obtain the accuracy of this model application, it was compared with saturated water content model and seepage force model. The comparison results of the three models showed that the simulation results of this model are best matching with the observation data. Moreover, the verification and validation indicate that our proposed model can be used to effectively analyze the rainfall infiltration of road slope.

Keywords: landslides; rainfall infiltration; PFC^{3D}; moisture content; earth pressure; comparison



Citation: Gu, X.; Nie, W.; Li, Q.; Geng, J.; Zhou, T.; Yuan, C. Discrete Element Simulation of the Road Slope Considering Rainfall Infiltration. *Water* **2022**, *14*, 3663. <https://doi.org/10.3390/w14223663>

Academic Editor: Renato Morbidelli

Received: 11 October 2022

Accepted: 8 November 2022

Published: 13 November 2022

Publisher's Note: MDPI stays neutral with regard to jurisdictional claims in published maps and institutional affiliations.



Copyright: © 2022 by the authors. Licensee MDPI, Basel, Switzerland. This article is an open access article distributed under the terms and conditions of the Creative Commons Attribution (CC BY) license (<https://creativecommons.org/licenses/by/4.0/>).

1. Introduction

Landslide disasters induced by rainfall are one of the main natural disasters faced by China. They cause immeasurable personal safety injury and property damage to surrounding residents [1–3]. Rainfall infiltration in soil bring about changes in the water content, soil mass and shear strength of slope, which may further affect its stability [4–8].

Physical model tests, by setting monitoring points, observe the changes in monitoring data after rainfall. They can infer the regulation between internal rainwater flow and landslide damage [9–12]. This method may intuitively obtain the deformation trend of slope, but the variation of soil moisture cannot be clearly recognized only by setting several monitoring points. Thus, it is difficult to accurately grasp the overall water diversion path of slope [13].

For this challenge, numerical model is effective. The moisture, stress and displacement of soil are simulated by defining the mechanical parameters in the numerical model [14–18]. The particle flow discrete element method is an optional method to study rainfall infiltration on slopes. Different properties of discrete media can be used to study the macroscopic behavior of soil under different conditions [19,20].

At present, there are two prime methods to simulate the influence of rainfall infiltration on slopes by using discrete element software: (1) Coupling. For example, CFD-DEM coupling and PFC-FLAC coupling. The former realizes the flow field by creating a background grid. Its fluid-particle interaction forces are calculated by updating the fluid element parameters [21–24]. The latter is first used to calculate the flow field in FLAC, and then

imported into PFC for seepage force simulation [25–28]. (2) Simplify the rainfall process. The effects of rainfall infiltration are equivalent to using saturation parameters, adding seepage force and reducing friction force [29–33].

These methods can be used to simulate rainfall infiltration process of slopes. In other words, the process of catastrophe can be analyzed to a certain extent. By contrast, there are also two shortcomings: First of all, it is difficult to establish a flow field with a complex shape by DEM model [34]. Currently, CFD—DEM simulation technology has achieved a leap from two-dimensional (2D) to three-dimensional (3D). It has been increasingly applied in the geotechnical engineering field. However, most of the research technology is based on structured grids. In detail, the simulated flow field is very regular and monotonous (e.g., square or cylinder). For large-scale engineering with complex shapes, it is still difficult to carry out numerical simulations. Moreover, simplified rainfall models do not yield moisture and intensity changes within the slope [35].

In this study, PFC^{3D} software [36] was used to develop a rainfall infiltration model for slopes by integrating moisture transfer, intensity decay, and seepage force methods. The model is validated by comparing moisture content monitoring data with simulation results. In addition, to obtain the applicability of the infiltration model, retaining wall pressure monitoring is conducted on a road slope in Nanping City, Fujian Province, China [37]. Ultimately, the simulation results of our proposed model are compared with saturated water content model and seepage force model.

2. Materials and Methods

To simulate the infiltration process, the water content property was added to the discrete unit. Darcy's law [38] was introduced to calculate the hydraulic gradient values of adjacent particles. A functional relationship between water content and shear strength was added to infiltration process. Then, the magnitude of seepage force was associated with the distribution of the water content. Finally, the moisture field and stress field of the road slope were obtained by circular calculation (Figure 1).

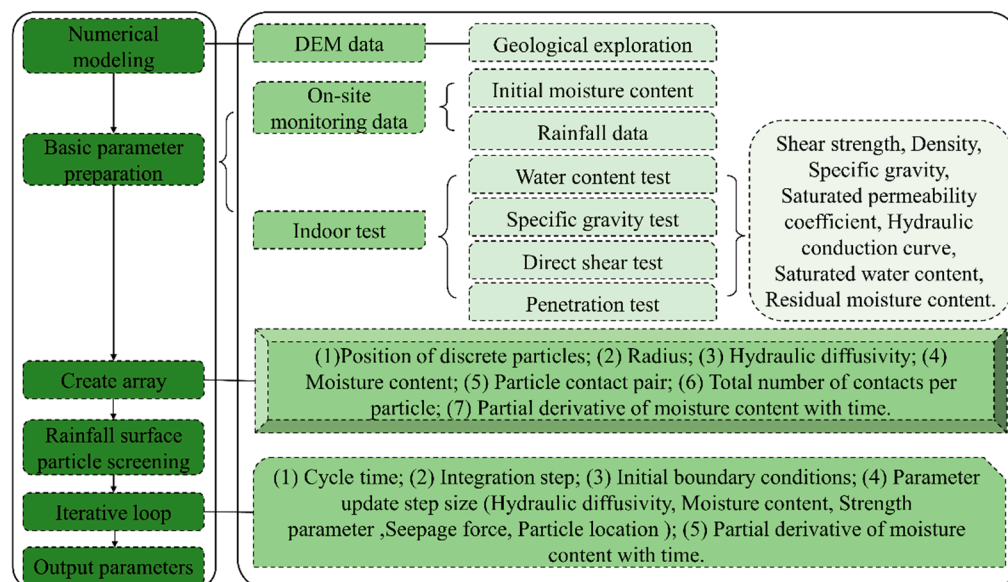


Figure 1. Rainfall infiltration simulation flow.

2.1. Moisture Diffusion Model

According to previous studies [39–41], the following assumptions are used to describe the water flow process in the discrete element: (1) each discrete particle carries unsaturated flow information (water diffusion rate, volume water content). The particle volume and surrounding porosity can form an equivalent continuous space. (2) when the pressure head or volumetric water content between adjacent particles is different, unsaturated infiltration

will occur. Moisture is transported at the contact points of discrete elements. Water flows from particles with high water content to particles with low water content. This assumption can explain the process of water diffusion microscopically, which is a simplification of the seepage process.

The water content of the fluid flowing in and out of the particle conforms to the continuity equation and Darcy's law. For multi-dimensional flow, the appropriate form of the flow equation is [42]:

$$\frac{\partial \theta}{\partial t} = -\nabla \cdot \mathbf{q} \quad (1)$$

where θ is the volumetric water content, t is time, \mathbf{q} is the water-flux vector.

Consider a particle i , which has N contacts with the surroundings. Assume that the surrounding contact particles of particle i are $j, j+1, j+2, j+\dots, j+N$. Using Darcy's law, the volumetric water content of particle i can be calculated as follows [42]:

$$\frac{\partial \theta_i}{\partial t} = \frac{1}{V_i} \sum_{j=1}^N d_{ij} \frac{\Delta \theta_{ij}}{L_{ij}} \quad (2)$$

where θ_i is the volumetric water content particle i , V_i is the equivalent continuous space volume, d_{ij} is the moisture diffusion rate between particles i and j , the distance between the contact point of particle i and particle j is L_{ij} , and the difference in water content is $\Delta \theta_{ij}$.

In our study, the water diffusivity of the particle can be calculated from the soil water retention curve and hydraulic conductivity curve [43]:

$$D = \frac{(1-m)K_s}{\alpha m(\theta_s - \theta_r)} S_e^{(\frac{1}{2} - \frac{1}{m})} \left[\left(1 - S_e^{\frac{1}{m}}\right)^{-m} + \left(\left(1 - S_e^{\frac{1}{m}}\right)^m\right) - 2 \right] \quad (3)$$

where D is the diffusion rate, θ_s is the saturated volume water content; θ_r is the residual water content, K_s is the saturated permeability coefficient, α , m and n are three fitting parameters, and S_e is the effective saturation ($S_e = \frac{\theta_i - \theta_r}{\theta_s - \theta_r}$).

The diffusion rate between particle i and the surrounding contact particles is [39]:

$$d_{ic} = \frac{3D(\theta_i)V_i}{\sum_{j=1}^N L_{ic}} \quad (4)$$

where d_{ic} is the moisture diffusion rate between particle i and contact point c , $D(\theta_i)$ is the diffusion rate of particle i , and L_{ic} is the distance from the center of particle i to its contact point c .

With the contact point as the intermediate variable, the moisture diffusion between particles i and j can be calculated as follows [44]:

$$d_{ij} = \frac{2d_{ic}d_{jc}}{d_{ic} + d_{jc}} \quad (5)$$

The volume water content of particle i in Δt time can be calculated as follows [42]:

$$\theta_i^{t+\Delta t} = \theta_i^t + \Delta t \left(\frac{1}{V_i} \sum_{j=1}^N \frac{d_{ij}}{L_{ij}} \Delta \theta_{ij} \right) \quad (6)$$

In the process of water transfer, we need to ensure the conservation of water. For instance, if the moisture content of particle j becomes $(\theta_j + \Delta \theta)$, the water content of particle i will become $(\theta_i - \Delta \theta)$.

2.2. Strength Calculation between Particles

Soil shear strength decays with rainfall infiltration. Taking the linear contact model as an example, micromechanical parameters are characterized as K_n , K_s , and μ . In our test, the

mechanical properties are equivalent to the friction coefficient. The relationship between the water content and friction coefficient was studied. The relevant steps are as follows:

- (1) Samples are taken at the slope site, and 5–10 groups of samples with different water content are designed;
- (2) An indoor direct shear test is conducted for each group of experiments. The vertical pressure is divided into 50 kPa, 100 kPa and 200 kPa. The horizontal shear stress is applied under different vertical pressures to obtain the shear stress at failure;
- (3) A numerical model is established in PFC to simulate the direct shear test. Based on the water content grouping in step (1) and the shear strength obtained in step (2), the numerical simulation inversion can obtain the mapping relationship between the water content and friction coefficient;
- (4) Draw curves. Take the water content as the abscissa and the friction coefficient as the ordinate;
- (5) Fit the curve. A mathematical equation is obtained, which takes the water content as independent variable and friction coefficient as dependent variable;
- (6) Based on the fitting equation, the program in PFC is used to map the moisture transfer and friction coefficient of the particles.

2.3. Strength Calculation between Particles

This study considers the influence of seepage force on slope stability, and adds seepage force to discrete particles [45]. The seepage force of soil particles per unit volume can be expressed by the following formula [46]:

$$F = \gamma_w \times I \times V \quad (7)$$

where F is the seepage force, γ_w is the unit weight of water, 9.8 kN/m^3 . I is the hydraulic gradient, V is the equivalent continuous space volume, and the hydraulic gradient I can be calculated by the following formula:

$$I = \frac{\Delta H}{L} = \frac{\Delta \left[z + \frac{h}{\gamma_w} + \frac{v_w^2}{2g} \right]}{L} \quad (8)$$

where ΔH is the total head, L is infiltration path length, z is the location head, $\frac{h}{\gamma_w}$ is the pressure head, and $\frac{v_w^2}{2g}$ is the velocity head. During the infiltration process, the velocity head is usually small. To improve the calculation efficiency, the velocity head is simplified as 0.

According to the soil water retention curve, we can convert the volume water content and pressure head. When the pressure head u is known, the water retention curve is used to calculate the volume water content θ . Similarly, when the water content θ is known, the pressure head u can be inversely calculated [47].

$$S_e = \frac{\theta - \theta_r}{\theta_s - \theta_r} = \frac{1}{[1 + (\alpha |u|)^n]^m} \quad (9)$$

Combining the three Formulas (7)–(9), the seepage force of discrete particles can be obtained.

3. Application

3.1. Study Area

As shown in Figure 2, the study area is located next to Gaoyang road and belongs to Gaoyang Township, Shunchang County, Nanping City, Fujian Province, China. Gaoyang covers an area of 236.5 km^2 . It governs 13 administrative villages and a timber yard. Here, the climate is mild and rainfall is abundant throughout the year.

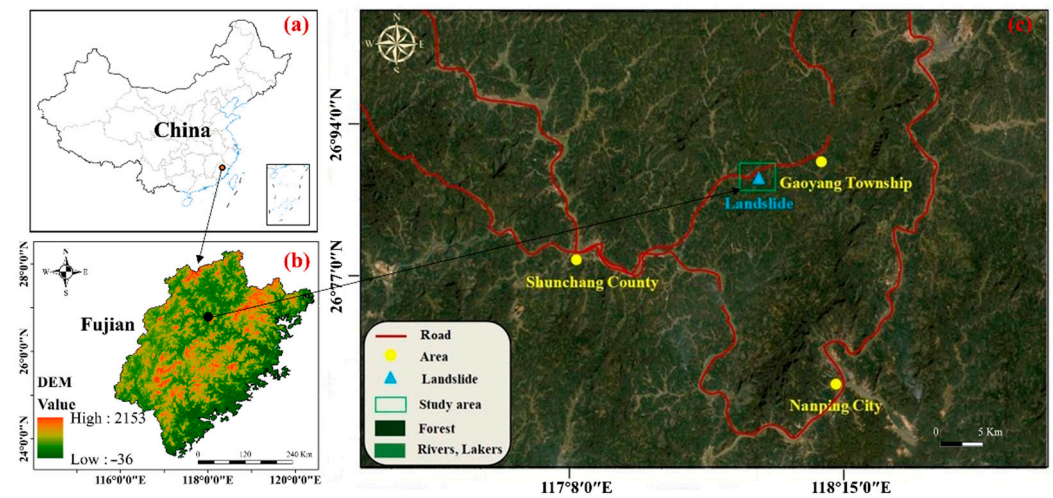


Figure 2. Location map of the Nanping road slope. (a) The location of Fujian in the whole country; (b) Nanping terrain; (c) The location of slope.

The slope is located in the traffic artery, surrounded by factories. The Gaoyang river lies in front. Its gradient is approximately 37° – 71° , and the surface is crisscrossed with gullies. If a high-intensity rainfall event occurs, it is prone to landslides [48]. This will greatly threaten the life safety of the surrounding residents, and will cause traffic congestion. See Figure 3 for the slope topography and surrounding layout.

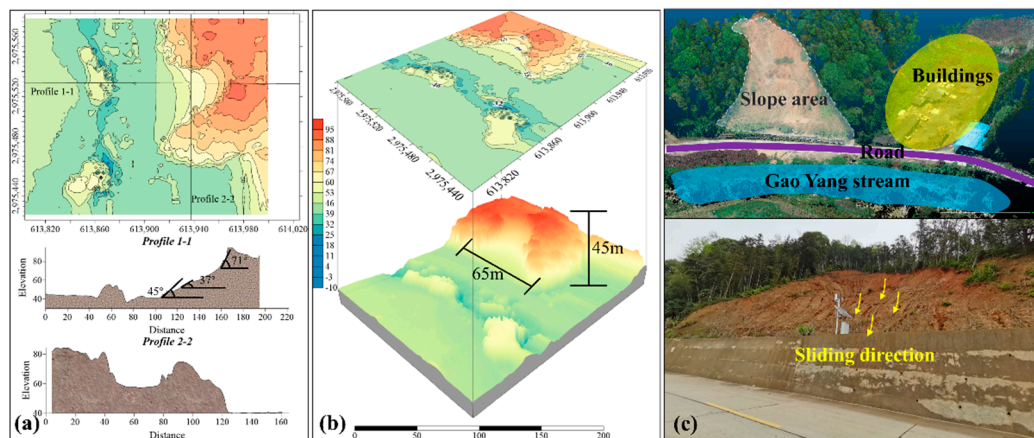


Figure 3. Topography and surrounding layout of the Nanping road slope. (a) Two sections of the slope in the north-south and east-west directions; (b) Slope size; (c) Distribution around the slope.

3.2. Slope Model and Boundary Conditions

High-precision slope images can be obtained by drones [49]. PhotoScan software is used to reconstruct 3D slopes. CloudCompare software is used for point cloud clipping. ArcGIS, AutoCAD, Rhinoceros are used for 3D modeling. As a result, they are imported into PFC^{3D} software to formative sliding bodies and sliding beds (Figure 4).

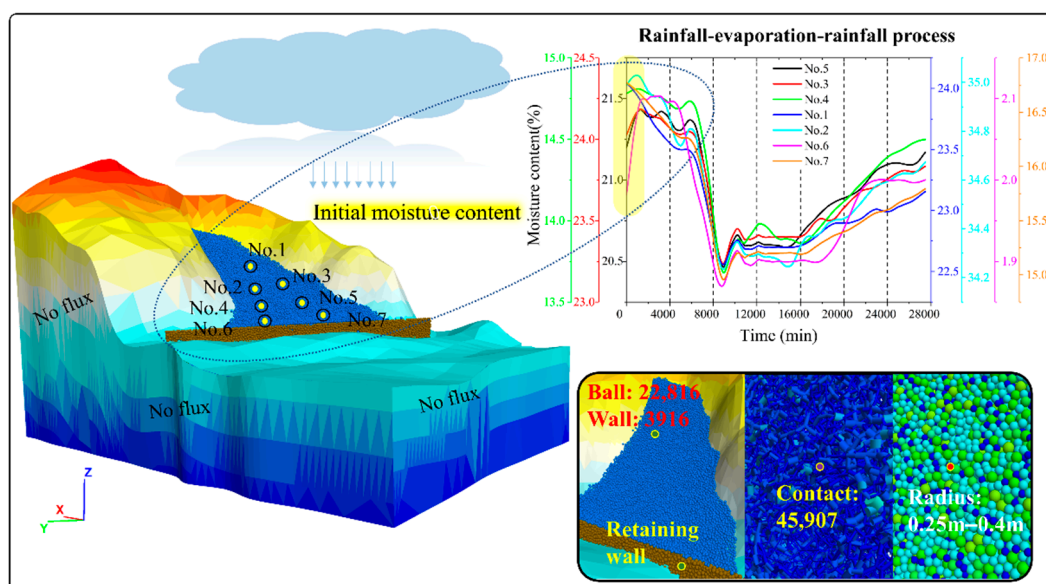


Figure 4. Slope model composition and initial boundary condition setting.

As shown in Figure 4, our numerical model size of the sliding body is 65 m long in the SN direction and 70 m wide in the EW direction. The maximum height difference of the model is approximately 45 m, which is basically consistent with the actual terrain. The sliding bed is mainly composed of triangular walls, with 3916 facets.

Particle radius in PFC^{3D} is limited by slope volume and computer performance. Considering the size effect and computer operation, the particle radius of this model was set to 0.25~0.4 m. The number of particles reaches 22,816 when the slope is calculated to be in equilibrium.

In addition, seven symmetrically distributed water content monitoring points (No. 1~7) are embedded in the slope because the topography of the slope is high on the left and low on the right. This design can obtain the distribution pattern of water content on both sides. Initial moisture content of the model is set based on seven moisture content sensors. The initial water content state of each part of the slope is shown in the curves in Figure 4 (No.1: 24.04%, No.2: 34.99%, No.3: 24.02%, No.4: 14.78%, No.5: 21.20%, No.6: 1.98%, No.7: 16.77%). Boundary at the bottom of the slope is constrained. In consideration of water seepage, except that the sliding body can transmit water, the boundary condition of the sliding bed is arranged as impermeable.

3.3. Parameter Calibration

Discrete element method running models with micromechanical parameters use the parameter calibration method to express the macroscopic phenomena with microscopic parameters [50–52]. There is no direct quantitative relationship between micro-parameters and macro-parameters. In general, various methods are used to calibrate the parameters to determine the micro-parameters of the model in PFC^{3D} [53–55].

In this study, the parameters are calibrated using indoor direct shear tests (Figure 5a). The DEM contacting mechanics model of road slope is built by direct shear test to adjust the particle micro-parameters. Then, the cohesive force $c = 1$ kPa and the internal friction angle $\Phi = 20^\circ$ of the soil are obtained. Comparing them with the shear strength obtained from the indoor experiments (Figure 5b), the mechanical parameters obtained from the simulations are very close to the macroscopic mechanical parameters obtained from the tests. In this way, micro parameters of the model are determined.

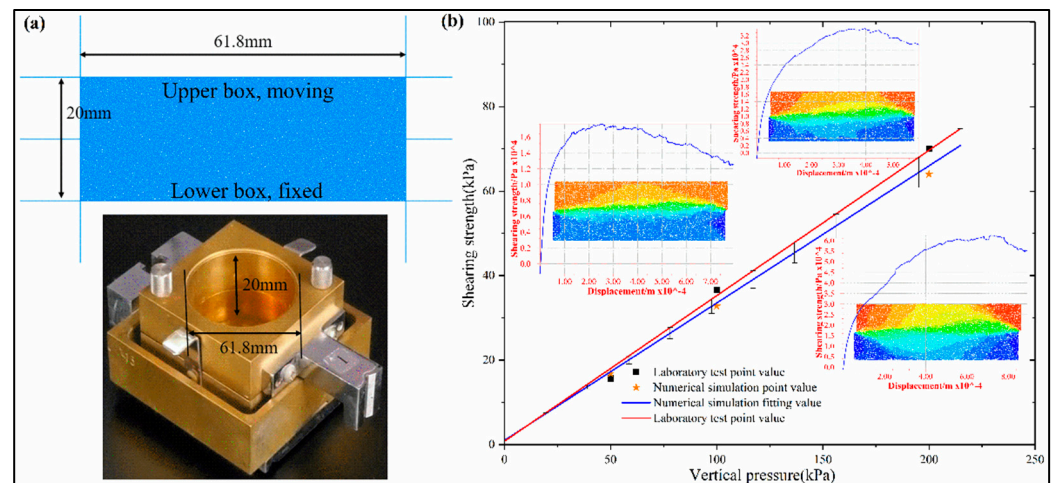


Figure 5. Parameter calibration process and results. (a) Numerical model of the direct shear test; (b) Parameter calibration result.

To obtain other relevant parameters of the rainfall infiltration model in Section 2.1, samples are taken at the slope site for the indoor test. These parameters include: saturated volume moisture content θ_s ; residual moisture content θ_r , saturated permeability coefficient K_s , and fitting parameters α , m , n . The parameters are as shown in Table 1.

Table 1. Soil mechanical parameters.

Parameters	Definition	Parameter Value
R	Radius (m)	0.25–0.4
ρ	Density (kg/m^3)	1600
k_s	Tangential stiffness (Pa)	5×10^7
k_n	Normal stiffness (Pa)	5×10^7
θ_s	Saturated volume moisture content	0.4
θ_r	Residual moisture content	0.008
K_s	Saturated permeability coefficient	2.46×10^{-6}
α, m, n	Fitting parameters	1.76, 4.53, 0.22

Based on the strength calculation steps in Section 2.2, the moisture content of the sample is divided into seven groups, namely 5%, 10%, 15%, 20%, 25%, 30% and 40%. Then, a combination of direct shear tests and numerical simulations is used to acquire the fitted equations. The functional relationship between water content and friction is as follows:

$$f = -0.0004w^2 + 0.018w + 0.4056 \quad (10)$$

where f is the friction force, and w is the moisture content, %.

4. Results and Discussion

4.1. Comparison of Moisture Content

This rainfall infiltration model is applied to the road slope. The soil particles are simulated by discrete units, and the moisture is transferred between discrete units (Figure 6a). The field water content monitoring data is adopted as the initial water condition of numerical model. Later, the slope is made to be relatively stable under the initial conditions. In this balanced state, the field rainfall data is input, and slope infiltration is implemented. To improve the efficiency of the simulation, we admit the flow direction of the whole slope as the seepage force direction; this means the direction along the slope toward the foot of the slope (Figure 6b).

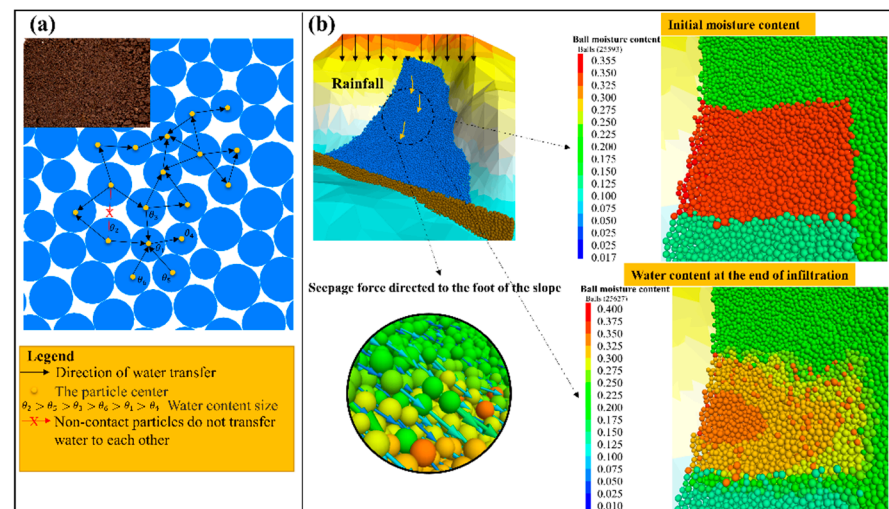


Figure 6. Water diffusion mechanism and seepage force direction. (a) is the water flow direction in the numerical model; (b) is the direction of seepage force and the distribution of water content of slope infiltration.

To verify the accuracy of this infiltration model, the monitored and simulated values of water content are compared based on the rainfall event of 27 April 2022. The rainfall intensity of the 4-h 21 mm total is input into the model, and the results are as shown in Figure 7.

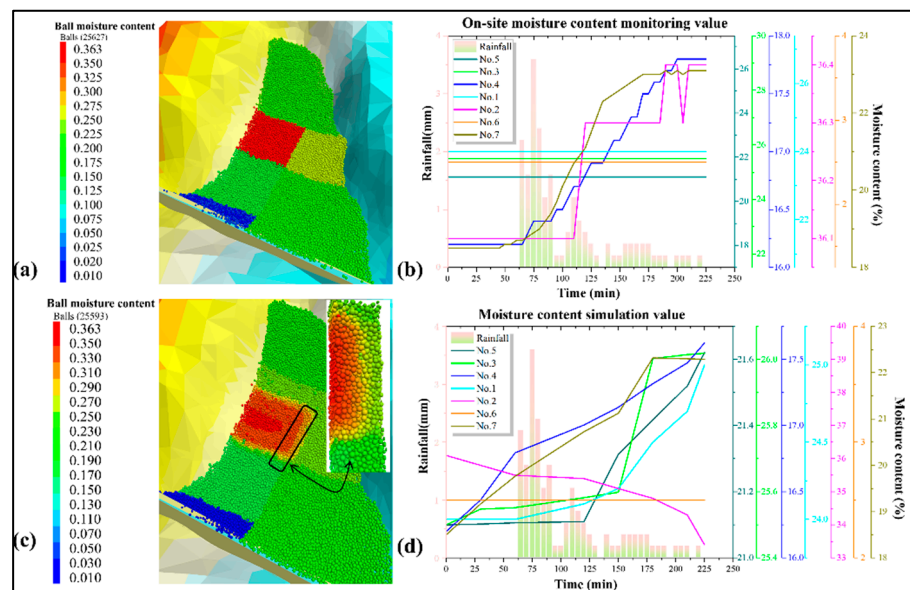


Figure 7. Comparison of field monitoring values and numerical simulation values of seven water content monitoring points. (a) Distribution of water content at the initial stage of rainfall; (b) Variation in water content on-site during a rainfall event; (c) Distribution of water content at the end of rainfall; (d) Water content change of numerical simulation during a rainfall event.

Results show that the tendencies of the other six points are consistent with the monitoring data, except for monitoring point 2. Under the effect of rainfall, the water content continues to increase. However, the trend of the curve at monitoring point 2 is opposite to the monitoring data. Returning to the rainfall level, it can be explained as follows: before implementing rainfall on the model, surface rainfall particles need to be selected. Due to the irregular shape of the slope, errors may occur when selecting surface rainfall particles. Therefore, when the moisture transfer was performed, monitoring point 2 not only did not

receive moisture, but also transferred moisture to the surrounding area because of the high water head. So, the moisture content of monitoring point 2 will have a tendency for data reduction. The error of numerical simulation results is calculated in this paper, and the results are as shown in Table 2.

Table 2. Comparison of water content results.

Rainfall Time	Rainfall Duration	Moisture Content Monitoring Point	No.1	No.2	No.3	No.4	No.5	No.6	No.7
27 April 2022	21 mm/4 h	Field monitoring (%)	24.00	36.40	25.50	17.80	21.20	2.50	20.30
		Numerical simulation (%)	25.00	33.37	26.02	17.62	21.62	2.50	22.29
		Relative error * (%)	4.17	8.32	2.04	1.01	1.98	0	9.8

Note: * The calculation method of relative error is: (Numerical simulation – Field monitoring)/Field monitoring $\times 100\%$.

As shown in Table 2, the results show that the water content data of seven points have little change in this rainfall, and the error of water content in numerical simulation is between 0–10%, which is basically consistent with the field monitoring data. It can be considered that the rainfall infiltration model is effective.

4.2. Earth Pressure Comparison

After the accuracy of our model was verified, the next step was to verify the availability of its impact on slope stability. Based on monitoring data from earth pressure gauges, the applicability of this model was compared with other rainfall models (see Figure 3 for the location of the retaining wall). In our study, the two most commonly used models for simulating rainfall using PFC software were selected. They are saturated water content model and seepage force model. Among them, the former uses saturated water content equivalent to the distribution state of the slope moisture content after rainfall. The latter uses seepage force to replace the force of rainfall on the slope.

Taking the rainfall event of 12 May 2022 as an example, the three models are simulated separately for the forces on the retaining wall. These simulated values were compared with the monitoring data to obtain the accuracy of the three models. The results are as shown in Figure 8.

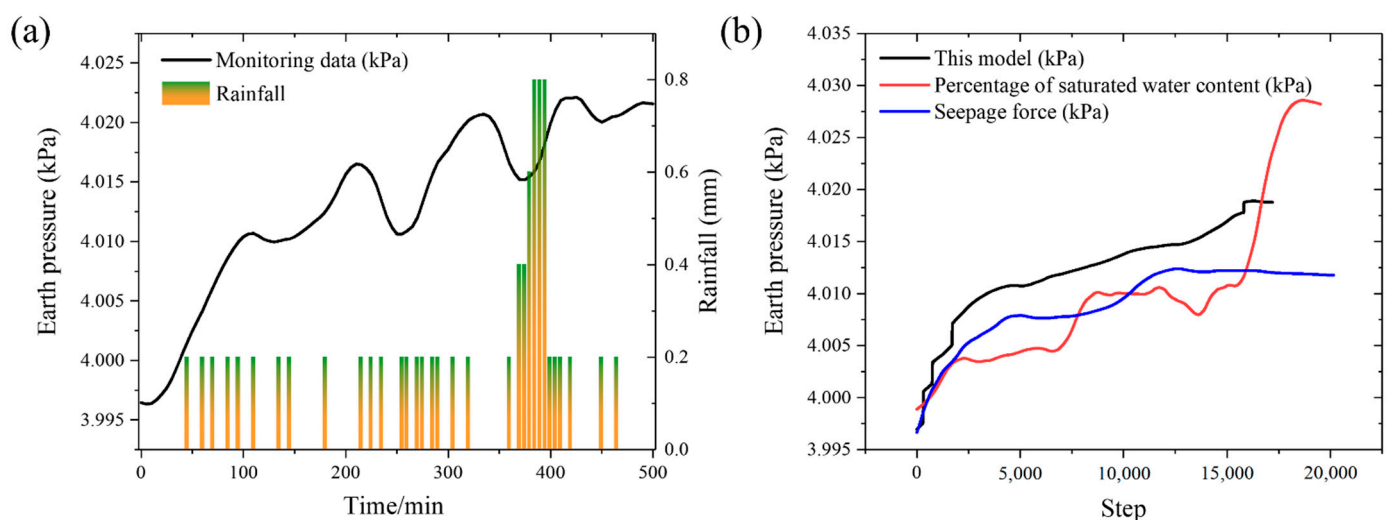


Figure 8. Comparison of the soil pressure results obtained by the three models. (a) The monitoring data; (b) The simulated data from three models.

As can be seen from Figure 8, the monitoring data and simulated data of retaining wall pressure show a steady growth tendency. Although the curve fluctuates, it eventually tends

to balance. In this paper, the initial value, final value, process value, error of monitoring data and simulation data are plotted in a table (Table 3). Compared with the monitoring data, the simulation accuracy of our proposed model, saturated water content model and permeability model are 11.5%, 17.82% and 38.99%, respectively. The simulation accuracy of our proposed model is higher than the other two models. Thus, results show the rainfall infiltration model combined with water transfer rules, strength calculation and seepage force is more available in slope stability analysis.

Table 3. Summary of soil pressure results simulated by three models.

Value	Monitoring Data	Simulated Data			Relative Error *		
		This Model	Saturated Water Content Model	Seepage Force Model	This Model	Saturated Water Content Model	Seepage Force Model
Start value	3.99667	3.99639	3.99857	3.99667			
Peak value	4.02214	4.01891	4.02858	4.01221	11.5%	17.82%	38.99%
Difference value	0.02547	0.02252	0.03001	0.01554			

Note: * The calculation method of relative error is: (simulated value – monitored value)/monitored value × 100%.

4.3. Highlights and Prospects

The equivalent rainfall method and coupling method are commonly used in the discrete element analysis of slope rainfall infiltration. There are few studies on the combination of multivariate factors. In this study, a rainfall infiltration model integrating water transfer, intensity decay and seepage force is proposed to emerge the rainfall infiltration process.

We systematically reviewed and analyzed the rainfall model, which has the following advantages compared with previous models: (1) Presenting the distribution pattern of moisture content; (2) Obtaining the functional relationship between shear strength and water content; (3) Calculating the seepage force at different times. Furthermore, we compared the model with the actual monitoring data of the slope. Results showed the simulated value of water content is close to the monitored value in the process of water transfer. In terms of influence on slope stability, the variation value of our proposed model is similar to that of in-situ earth pressure monitoring.

Of course, our proposed model still has great optimization potential: (1) There is no systematic identification method for screening surface rainfall particles. Due to the irregularity of the slope shape, we selected the particles simply by the number of contacts. This will lead to incomplete particle screening, and may result in screening too many particles. As a result, the accuracy of subsequent water transfer is affected. A code is planned to be developed to solve the recognition of surface particles and achieve accurate coverage of rainfall on irregular slope surfaces. (2) In terms of seepage force, theoretically, in the process of water diffusion, the diffusion direction is the direction of seepage force. However, to improve the calculation efficiency, this paper unifies the direction of the seepage force to point to the toe of the road slope, which may affect the subsequent slope stability calculation. We plan to balance the calculation efficiency with the direction of seepage force, estimate the influence of seepage force direction to slope stability and reduce the error caused by it. (3) For the initial water content distribution, we divided seven zones according to the distribution of water content sensors, which is somewhat different from the water content distribution of the actual slope. There is a phenomenon of water transfer between each area even without rainfall, which will affect the subsequent slope stability calculation. Subsequently, we plan to match the water content with the slope location to minimize the influence of the initial water content distribution on the slope stability.

5. Conclusions

This study shows a rainfall infiltration model implemented on a road slope in Nanping City, Fujian Province, China. Compared to previous models, the proposed model integrates water transfer, intensity decay and seepage force methods. Water content visualization,

intensity mapping and seepage force effects are achieved. By introducing water content properties, combined with water diffusion coefficients, water transfer to the slope is analyzed. This can visually and comprehensively show the water content status of the slope before and after rainfall. Based on the direct shear test, the functional relationship between shear strength and water content can be quickly obtained. Not only that, the moisture distribution is combined with the calculation of seepage force to realize the force of rainfall on the slope body. Furthermore, the accuracy of our proposed model is good as verified by the field monitoring data. In terms of water content, the comparison error is 0–10%. In the aspect of soil pressure, the simulation accuracy of our proposed model, saturated water content model and seepage force model are 11.5%, 17.82% and 38.99%, respectively. We believe that this rainfall infiltration model can be a great reference for the study of rainfall-induced slope stability.

Author Contributions: Conceptualization, X.G. and W.N.; Data curation, X.G., Q.L. and C.Y.; Formal analysis, Q.L.; Funding acquisition, W.N.; Investigation, Q.L. and J.G.; Methodology, X.G. and T.Z.; Project administration, W.N.; Resources, W.N.; Software, X.G., T.Z. and C.Y.; Supervision, W.N. and J.G.; Validation, X.G. and W.N.; Visualization, X.G. and T.Z.; Writing—original draft, X.G.; Writing—review & editing, W.N. All authors have read and agreed to the published version of the manuscript.

Funding: This research was funded by Excellent Youth Foundation of Jiangxi Scientific Committee (20212ACB214005), Fujian Province Science and Technology Plan Project (2022T3051), the Graduate Research and Innovation Foundation of Chongqing, China (CYB20023) and National Natural Science Foundation of China (52064016).

Data Availability Statement: The datasets used and analyzed during the current study are available from the corresponding authors upon reasonable request.

Acknowledgments: The authors express their gratitude to Li Yuyang and Zhu Tianqiang from Jiangxi University of Science and Technology for their help in the field research work.

Conflicts of Interest: The authors declare no conflict of interest.

References

- Sharma, R.H.; Shaky, N.M. Rain induced shallow landslide hazard assessment for ungauged catchments. *Hydrogeol. J.* **2008**, *16*, 871–877. [\[CrossRef\]](#)
- Chenguang, W.U.; Meng, L.U.; Jie, Z.; Jiang, Z. Probabilistic Prediction of Rain-Induced Landslide Travel Distance. *J. Eng. Geol.* **2019**, *27*, 164–171.
- Bhardwaj, A.; Wasson, R.J.; Ziegler, A.D.; Chow, W.T.L.; Sundriyal, Y.P. Characteristics of rain-induced landslides in the Indian Himalaya: A case study of the Mandakini Catchment during the 2013 flood. *Geomorphology* **2019**, *330*, 100–115. [\[CrossRef\]](#)
- Cho, S.E. Stability analysis of unsaturated soil slopes considering water-air flow caused by rainfall infiltration. *Eng. Geol.* **2016**, *211*, 184–197. [\[CrossRef\]](#)
- Damiano, E.; Greco, R.; Guida, A.; Olivares, L.; Picarelli, L. Investigation on rainwater infiltration into layered shallow covers in pyroclastic soils and its effect on slope stability. *Eng. Geol.* **2017**, *220*, 208–218. [\[CrossRef\]](#)
- Zhang, J.; Zhu, D.; Zhang, S. Shallow slope stability evolution during rainwater infiltration considering soil cracking state. *Comput. Geotech.* **2020**, *117*, 103285. [\[CrossRef\]](#)
- Li, Q.; Song, D.; Yuan, C.; Nie, W. An image recognition method for the deformation area of open-pit rock slopes under variable rainfall. *Measurement* **2022**, *188*, 110544. [\[CrossRef\]](#)
- Morbidelli, R.; Saltalippi, C.; Flammini, A.; Govindaraju, R.S. Role of slope on infiltration: A review. *J. Hydrol.* **2018**, *557*, 878–886. [\[CrossRef\]](#)
- Li, M.; Zhang, X.; Yang, Z.; Yang, T.; Pei, X. The rainfall erosion mechanism of high and steep slopes in loess tablelands based on experimental methods and optimized control measures. *Bull. Eng. Geol. Environ.* **2020**, *79*, 4671–4681. [\[CrossRef\]](#)
- Tan, W.; Huang, Q.; Chen, X. Physical Model Test on the Interface of Loess Fill Slope. *Land* **2022**, *11*, 1372. [\[CrossRef\]](#)
- Wang, H.; Jiang, Z.; Xu, W.; Wang, R.; Xie, W. Physical model test on deformation and failure mechanism of deposit landslide under gradient rainfall. *Bull. Eng. Geol. Environ.* **2022**, *81*, 66. [\[CrossRef\]](#)
- Li, Q.; Geng, J.; Song, D.; Nie, W.; Saffari, P.; Liu, J. Automatic recognition of erosion area on the slope of tailings dam using region growing segmentation algorithm. *Arab. J. Geosci.* **2022**, *15*, 438. [\[CrossRef\]](#)
- Zhu, W.; Ren, M.; Dai, F.; Zhang, P.; Wang, L.; Liu, H.; Jia, H.; Wang, X. Prediction and Early Warning of Mining-induced Disasters Based on Combined In-situ Monitoring and Numerical Simulation. *Met. Mine* **2020**, *52*, 151–162.

14. Su, Z.; Wang, G.; Wang, Y.; Luo, X.; Zhang, H. Numerical simulation of dynamic catastrophe of slope instability in three Gorges reservoir area based on FEM and SPH method. *Nat. Hazards* **2022**, *111*, 709–724. [\[CrossRef\]](#)
15. Wang, Z.; Li, Q.; Zhang, N.; Jin, Y.; Qin, H.; Ding, J. Slope failure of biotreated sand embankments under rainfall conditions: Experimental investigation and numerical simulation. *Bull. Eng. Geol. Environ.* **2020**, *79*, 4683–4699. [\[CrossRef\]](#)
16. Guo, Z.; Zhao, Z. Numerical analysis of an expansive subgrade slope subjected to rainfall infiltration. *Bull. Eng. Geol. Environ.* **2021**, *80*, 5481–5491. [\[CrossRef\]](#)
17. Elkamhawy, E.; Wang, H.; Zhou, B.; Yang, Z. Failure mechanism of a slope with a thin soft band triggered by intensive rainfall. *Environ. Earth Sci.* **2018**, *77*, 340. [\[CrossRef\]](#)
18. Joe, E.J.; Ali, N.; Jusoh, S.N. Numerical modelling of coupled seepage-deformation subjected to rainfall infiltration in unsaturated slope. *World J. Eng.* **2020**, *17*, 867–875. [\[CrossRef\]](#)
19. Tian, Y.; Wu, Y.; Lin, J.; Li, X.; Xu, D.; Zhou, F.; Feng, Q. Characterization of the Erosion Damage Mechanism of Coal Gangue Slopes through Rainwater Using a 3D Discrete Element Method: A Case Study of the Guizhou Coal Gangue Slope (Southwestern China). *Appl. Sci.* **2022**, *12*, 8548. [\[CrossRef\]](#)
20. Chang, W.; Wang, P.; Wang, H.; Chai, S.; Yu, Y.; Xu, S. Simulation of the Q2 loess slope with seepage fissure failure and seismic response via discrete element method. *Bull. Eng. Geol. Environ.* **2021**, *80*, 3495–3511. [\[CrossRef\]](#)
21. Hu, J.; Ma, T.; Ma, K. DEM-CFD simulation on clogging and degradation of air voids in double-layer porous asphalt pavement under rainfall. *J. Hydrol.* **2021**, *595*, 126028. [\[CrossRef\]](#)
22. Zhang, H.; Zhang, B.; Wu, C.; Chen, K. Macro and micro analysis on coal-bearing soil slopes instability based on CFD-DEM coupling method. *PLoS ONE* **2021**, *16*, e0257362. [\[CrossRef\]](#) [\[PubMed\]](#)
23. Zhang, Y.; Chen, J.; Zhou, F.; Bao, Y.; Yan, J.; Zhang, Y.; Li, Y.; Gu, F.; Wang, Q. Combined numerical investigation of the Gangda paleo landslide runout and associated dam breach flood propagation in the upper Jinsha River, SE Tibetan Plateau. *Landslides* **2022**, *19*, 941–962. [\[CrossRef\]](#)
24. Wang, Y.; Chai, J.; Xu, Z.; Qin, Y.; Wang, X. Numerical Simulation of the Fluid–Solid Coupling Mechanism of Internal Erosion in Granular Soil. *Water* **2020**, *12*, 137. [\[CrossRef\]](#)
25. Jiang, W.-Z.; Tan, Y.; Cao, Y.-C. Numerical Analyses of Erosion in Sand-Gravel Mixtures Caused by Buried Defective Pipeline under Intense Rainfall. In *Geo-Extreme*; American Society of Civil Engineers: Reston, VA, USA, 2021; pp. 150–159.
26. Hung, C.; Liu, C.-H.; Chang, C.-M. Numerical Investigation of Rainfall-Induced Landslide in Mudstone Using Coupled Finite and Discrete Element Analysis. *Geofluids* **2018**, *2018*, 9192019. [\[CrossRef\]](#)
27. Su, H.; Fu, Z.; Gao, A.; Wen, Z. Particle Flow Code Method-Based Meso-scale Identification for Seepage Failure of Soil Levee. *Transp. Porous Med.* **2017**, *119*, 311–336. [\[CrossRef\]](#)
28. Su, H.; Li, H.; Zhang, L.; Wen, Z. Particle flow code method-based seepage behavior analysis and control effect evaluation for soil levee. *Eng. Comput.* **2020**, *36*, 97–114. [\[CrossRef\]](#)
29. Li, W.C.; Li, H.J.; Dai, F.C.; Lee, L.M. Discrete element modeling of a rainfall-induced flowslide. *Eng. Geol.* **2012**, *149*, 22–34. [\[CrossRef\]](#)
30. Yang, G.; Qin, Y.; Jiang, W.; Liang, F.; Xiang, X. Characteristics and particle flow simulation of failure mechanism of Ludaping landslide in Renhuai red bed area, China. *Arab. J. Geosci.* **2022**, *15*, 1237. [\[CrossRef\]](#)
31. Lo, C.-M.; Lee, C.-F.; Huang, W.-K. Failure mechanism analysis of rainfall-induced landslide at Pingguang stream in Taiwan: Mapping, investigation, and numerical simulation. *Environ. Earth Sci.* **2016**, *75*, 1422. [\[CrossRef\]](#)
32. Zhang, C.; Wang, B.; Yang, Z.; Ji, E. Numerical Study on Vertical and Horizontal Seepage Deformation of Silty Soil. *IOP Conf. Ser. Earth Environ. Sci.* **2019**, *304*, 052099. [\[CrossRef\]](#)
33. Su, Y.; Lan, S.M.; Xu, L.; Ding, J.H. Simulation of Progressive Failure Process in Rainfall-Induced Landslides. *Adv. Mater. Res.* **2014**, *1065*, 63–66. [\[CrossRef\]](#)
34. Li, X.; Lu, Y.; Wu, Y. Application of CFD—DEM coupling method in seepage—induced ground subsidence. *J. Shanghai Univ. Nat. Sci. Ed.* **2020**, *26*, 842–852.
35. Liu, J.; Liu, Y.; Hu, Q. Stability of embankment slope subjected to rainfall infiltration considering both runoff-underground seepage and fluid-solid coupling. *Rock Soil Mech.* **2010**, *31*, 903–910.
36. *Itasca PFC (Particle Flow Code) Version 5.0*; Itasca Consulting Group Inc.: Chicago, IL, USA, 2014.
37. Weng, M.-C.; Lin, M.-L.; Lo, C.-M.; Lin, H.-H.; Lin, C.-H.; Lu, J.-H.; Tsai, S.-J. Evaluating failure mechanisms of dip slope using a multiscale investigation and discrete element modelling. *Eng. Geol.* **2019**, *263*, 105303. [\[CrossRef\]](#)
38. Whitaker, S. Flow in porous media I: A theoretical derivation of Darcy's law. *Transp. Porous Med.* **1986**, *1*, 3–25. [\[CrossRef\]](#)
39. Tran, K.M.; Bui, H.H.; Nguyen, G.D. DEM modelling of unsaturated seepage flows through porous media. *Comp. Part. Mech.* **2022**, *9*, 135–152. [\[CrossRef\]](#)
40. Tran, K.M.; Bui, H.H.; Nguyen, G.D. A hybrid discrete-continuum approach to model hydro-mechanical behaviour of soil during desiccation. *arXiv* **2021**, arXiv:2106.04676.
41. Gili, J.A.; Alonso, E.E. Microstructural deformation mechanisms of unsaturated granular soils. *Int. J. Numer. Anal. Meth. Geomech.* **2002**, *26*, 433–468. [\[CrossRef\]](#)
42. Hillel, D. Water Flow in Saturated Soil. In *Introduction to Environmental Soil Physics*; Elsevier: Amsterdam, The Netherlands, 2003; pp. 127–148.

43. Van Genuchten, M.T. A Closed-form Equation for Predicting the Hydraulic Conductivity of Unsaturated Soils. *Soil Sci. Soc. Am. J.* **1980**, *44*, 892–898. [[CrossRef](#)]
44. Berg, P. Long-term simulation of water movement in soils using mass-conserving procedures. *Adv. Water Resour.* **1999**, *22*, 419–430. [[CrossRef](#)]
45. Wang, X.; Xiao, L.; Zhao, J.; Ye, S.; Wei, J.; Huang, X. Analysis of the formation mechanism of a landslide in the lacustrine sediment of the Diexi ancient dammed lake in the upper reaches of the Minjiang River. *Bull. Eng. Geol. Environ.* **2022**, *81*, 339. [[CrossRef](#)]
46. Pan, Y.-W.; Su, H.-K.; Liao, J.-J.; Huang, M.-W. Reconstruction of Rainfall-induced Landslide Dam by Numerical Simulation—The Barrier Lake in Taimali River as an Example. In Proceedings of the ISRM International Symposium—8th Asian Rock Mechanics Symposium, Sapporo, Japan, 14–16 October 2014.
47. Brooks, R.H.; Corey, A.T. Properties of Porous Media Affecting Fluid Flow. *J. Irrig. Drain. Div.* **1966**, *92*, 61–88. [[CrossRef](#)]
48. Xie, W.; Nie, W.; Saffari, P.; Robledo, L.F.; Descote, P.-Y.; Jian, W. Landslide hazard assessment based on Bayesian optimization–support vector machine in Nanping City, China. *Nat. Hazards* **2021**, *109*, 931–948. [[CrossRef](#)]
49. Li, X.; Li, Q.; Hu, Y.; Chen, Q.; Peng, J.; Xie, Y.; Wang, J. Study on Three-Dimensional Dynamic Stability of Open-Pit High Slope under Blasting Vibration. *Lithosphere* **2022**, *2021*, 6426550. [[CrossRef](#)]
50. Ajamzadeh, M.R.; Sarfarazi, V.; Haeri, H.; Dehghani, H. The effect of micro parameters of PFC software on the model calibration. *Smart Struct. Syst.* **2018**, *22*, 643–662.
51. Wu, H.; Dai, B.; Zhao, G.; Chen, Y.; Tian, Y. A Novel Method of Calibrating Micro-Scale Parameters of PFC Model and Experimental Validation. *Appl. Sci.* **2020**, *10*, 3221. [[CrossRef](#)]
52. Ren, J.; Xiao, M.; Liu, G. Rock Macro–Meso Parameter Calibration and Optimization Based on Improved BP Algorithm and Response Surface Method in PFC 3D. *Energies* **2022**, *15*, 6290. [[CrossRef](#)]
53. Xia, L.; Zeng, Y. Parametric study of smooth joint parameters on the mechanical behavior of transversely isotropic rocks and research on calibration method. *Comput. Geotech.* **2018**, *98*, 1–7. [[CrossRef](#)]
54. Zhai, S.; Zhan, J.; Ba, Y.; Chen, J.; Li, Y.; Li, Z. PFC model parameter calibration using uniform experimental design and a deep learning network. *IOP Conf. Ser. Earth Environ. Sci.* **2019**, *304*, 032062. [[CrossRef](#)]
55. Su, H.; Li, H.; Hu, B.; Yang, J. A Research on the Macroscopic and Mesoscopic Parameters of Concrete Based on an Experimental Design Method. *Materials* **2021**, *14*, 1627. [[CrossRef](#)] [[PubMed](#)]